(Received 19 November 2024, Accepted 19 December 2024, Scheduled 21 December 2024)

Dual Non-Diffractive Beam Generation via Spin-and-Frequency Multiplexed All-Dielectric Metasurfaces

Chunyu Liu[1], Yanfeng Li[1,*], Fan Huang[1], Guanghong Xu[2], Quan Li[2], Shuang Wang[2], Quan Xu[1], Jianqiang Gu[1], and Jiaguang Han[1,3]

[1] *Center for Terahertz Waves, Key Laboratory of Optoelectronics Information and Technology (Ministry of Education of China) College of Precision Instrument and Optoelectronics Engineering, Tianjin University, Tianjin 300072, China*
[2] *School of Electronic Engineering, Tianjin University of Technology and Education, Tianjin 300222, China*
[3] *Guangxi Key Laboratory of Optoelectronic Information Processing, School of Optoelectronic Engineering Guilin University of Electronic Technology, Guilin 541004, China*

ABSTRACT: Metasurfaces offer remarkable capabilities for manipulating electromagnetic waves and by incorporating multiplexing techniques can significantly increase the versatility of design possibilities. Here, we designed and experimentally demonstrated a series of dual non-diffractive beam generators for terahertz radiation based on all-dielectric metasurfaces. These generators could produce switchable Bessel beams and abruptly autofocusing beams depending on the spin and frequency of the incident terahertz waves. In addition, by further applying appropriate phase gradients in the design, these non-diffractive beams could be deflected in specified directions. It is also possible to simultaneously generate multiple non-diffractive beams with different properties. The generated non-diffractive beams were measured with near-field scanning terahertz microscopy, and the results agreed well with simulations. We believe that these metasurface-based beam generators hold tremendous potential in terahertz imaging, communications, non-destructive evaluation, and many other applications.

1. INTRODUCTION

Non-diffractive beams are special types of light beams that, unlike Gaussian beams generated by conventional devices, can maintain stable propagation characteristics during transmission, unaffected by diffraction [1–5]. These beams are usually achieved through specific optical devices or specialized optical designs [6–9]. Non-diffractive beams have great potential in applications such as optical sensing [10], particle trapping [11], optical communications [12], just to name a few. The shape and intensity distribution of these beams are effectively maintained during propagation, making them widely adopted in applications requiring specific beam properties. Two distinctive types of non-diffractive beams are Bessel beams and abruptly autofocusing (AAF) beams. Bessel beams can maintain a constant intensity distribution over long distances during propagation [13, 14]. They consist of a central high-intensity spot surrounded by several concentric rings and find important applications in laser processing [15], optical tweezers [16], optical microscopy [17], and extended depth-of-field imaging [18]. AAF beams are non-diffractive beams characterized by initial low-energy propagation but with an abrupt significant energy increase near the designed focus. These beams initially have a ring-shaped pattern composed of a series of Airy beams around the center. During propagation, these Airy beams accelerate towards the center, gradually shrinking the ring-shaped pattern until it collapses into a point near the designed focus, resulting in a sharp increase in energy by several orders of magnitude [4, 5]. AAF beams are widely used in laser ablation [19], particle trapping [20], terahertz wave generation [21], light bullets [22], and many other fields. With the development of terahertz technology, non-diffractive beams have also found increasing applications in terahertz-related fields such as terahertz imaging [18, 23] and detection [24, 25].

Metasurfaces are two-dimensional metamaterials composed of subwavelength units, which can modulate the phase, amplitude, and polarization of incident electromagnetic waves [26–33]. These subwavelength units can possess complex geometries and have unique electromagnetic responses, thus enabling highly customized control over electromagnetic waves. As a result, metasurfaces demonstrate unprecedented capabilities in spectral modulation [34] and wavefront shaping [35–37]. In the spectrally important terahertz frequency range, as most natural materials are non-responsive to terahertz waves, and devices for wavefront shaping are highly desired, metasurfaces provide a highly effective solution. Metasurfaces based on dielectric materials (such as silicon) exhibit high transmission efficiency [38, 39], making them suitable for generating non-diffractive terahertz beams [40]. Additionally, the metasurface units can be designed to exhibit polarization [41] or frequency dependence [42]. Utilizing such units and by changing the polarization and/or frequency of the incident waves, the same metasurface can achieve different functionalities. Reported multiplexing devices are more common in the microwave [31, 33, 37] and optical [32, 42, 43] frequency ranges. For example, Huang et al. [44] reported a perfect vortex beam

* Corresponding author: Yanfeng Li (yanfengli@tju.edu.cn).

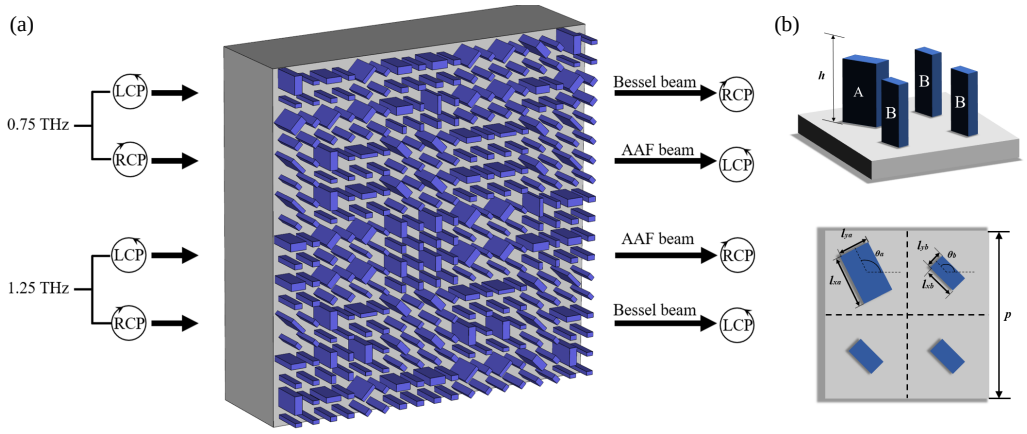

FIGURE 1. (a) Schematic diagram of a metasurface and illustration of the designed functions, and (b) side and top views of a meta-unit.

generator based on all-dielectric metasurfaces operating in the terahertz band, which utilizes spin multiplexing. However, it works at a single frequency. Devices capable of both frequency and spin multiplexing in the terahertz frequency range are still scarce and highly desirable.

In this work, we report spin-and-frequency multiplexed transmissive all-dielectric metasurfaces that can generate different non-diffractive beams under varying frequencies and incident polarization conditions. By superimposing the required phase functions, they can also produce deflected non-diffractive beams at specific angles and simultaneously generate multiple non-diffractive beams of different types. The devices operate at 0.75 THz and 1.25 THz, each offering unique functionalities and enabling frequency-dependent operation — a feature uncommon in conventional devices. They also exhibit polarization sensitivity, allowing different functionalities based on the polarization state of the incident waves. This dual-frequency and polarization-dependent capability enhances design flexibility, supporting the generation of Bessel beams with long non-diffractive propagation and AAF beams with abruptly concentrated energy during transmission, or both beams simultaneously. These metasurface devices provide a technique to generate combinations of non-diffractive beams, and the contrasting characteristics of these beams expand the potential of these devices in polarization- and frequency-dependent applications in the spectrally-important terahertz band.

The rest of this paper is organized as follows. The second section discusses the design of the metasurface. The third section presents the simulation results, while the fourth section details the experimental results and discussion. A final section draws the conclusions.

2. METASURFACE DESIGN

A spin-and-frequency multiplexed transmissive all-dielectric metasurface designed in this work is schematically shown in Fig. 1(a). We aim to achieve the following functionalities: When left-hand circularly polarized (LCP) light is incident on the metasurface, one type of beam is generated at a frequency of 0.75 THz, and another type of beam is generated at 1.25 THz; when the incident light is right-hand circularly polarized (RCP), the beams generated at 0.75 THz and 1.25 THz will differ from those produced by the LCP light, producing two switchable types of beams.

To achieve the desired spin-and-frequency multiplexing functionalities, we utilize polarization-dependent rectangular pillars on a silicon substrate as meta-units (Fig. 1(b)). The sub-wavelength unit arrays of the metasurface can be composed of pillars of different sizes. The initial phase distribution required to achieve the desired functionality is first calculated. Then, the basic units with different phase modulation capabilities are placed at corresponding positions, completing the design of a metasurface with specific functions. By altering the length and width of the rectangular pillars as well as their rotation angles, different effects can be achieved when LCP and RCP lights are incident onto the metasurface. This design is based on the superposition of the propagation phase and geometric phase [43, 44].

The propagation phase is altered by changing the length and width of the dielectric pillars, enabling independent control of the phase values of x- and y-polarized incident lights, which can be represented by φ_x and φ_y, respectively [40]. The geometric phase is modified by adjusting the rotation angle (denoted as α) of the dielectric pillars, which is used to control the phase of circularly polarized incident light: LCP (RCP) incident light is converted into RCP (LCP) light with an additional phase shift of -2α ($+2\alpha$) [45]. Therefore, geometric phase alone cannot independently control the phase of circularly polarized light with different polarization states. Propagation phase and geometric phase can be combined to achieve the independent phase control for circularly polarized light [43, 44]. Assuming pure phase control without the influence of amplitude, the required phase response for LCP incident light (converted to RCP light) is denoted as φ_{lr} and that for RCP incident light (converted to LCP light) as φ_{rl}. These two parameters and rotation angle can be constructed by [43]:

$$\begin{cases} \varphi_{lr}(x,y) = [\varphi_x(x,y) + \varphi_y(x,y)]/2 \\ \varphi_{rl}(x,y) = [\varphi_x(x,y) + \varphi_y(x,y)]/2 - \pi \\ \alpha = [\varphi_x(x,y) - \varphi_y(x,y)]/4 \end{cases} \quad (1)$$

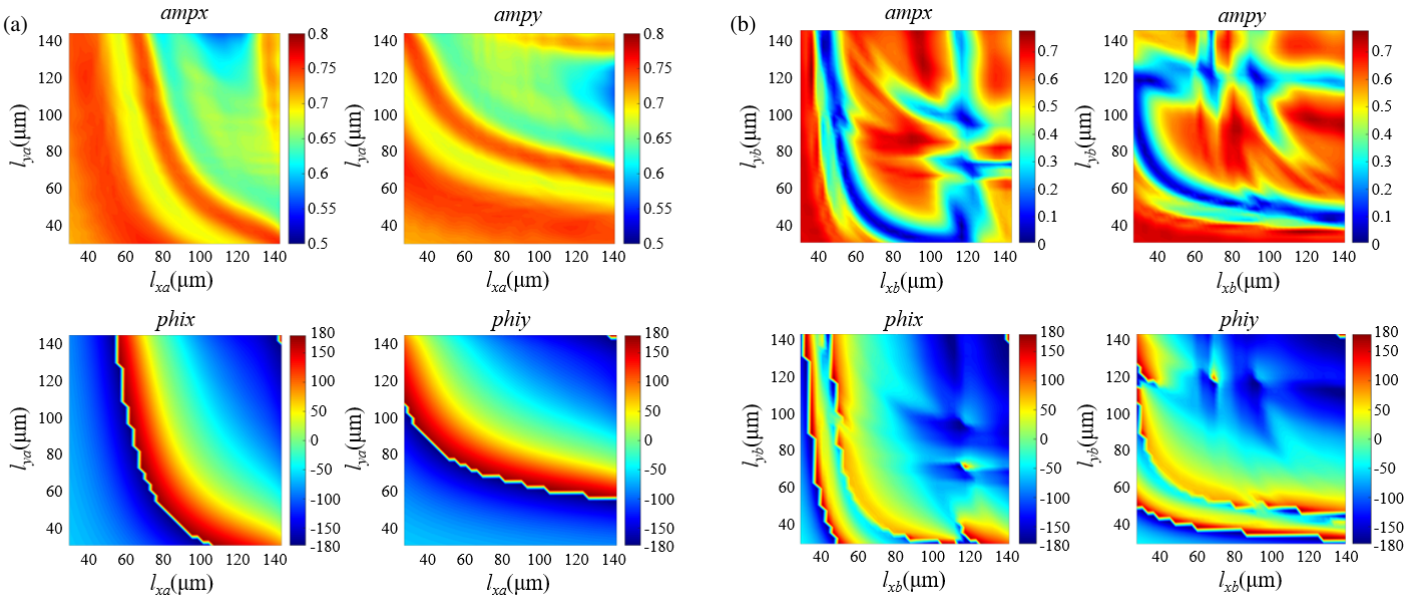

FIGURE 2. (a) Amplitude and phase modulation of 0.75 THz incident light as a function of l_{xa} and l_{ya}, and (b) amplitude and phase modulation of 1.25 THz incident light as a function of l_{xb} and l_{yb}. Here, *ampx* and *ampy* represent amplitude responses to x- and y-polarized incident light, respectively; *phix* and *phiy* represent phase responses to x- and y-polarized incident light, respectively.

As can be seen from Eq. (1), to independently control different circularly polarized lights, it is only necessary to calculate the phase distributions φ_x and φ_y required for the two linear polarization states. This equation will yield phase values φ_{lr} and φ_{rl}, as well as rotation angle α, corresponding to the desired functionalities. When the polarization state of the incident light is not circular polarization, it can be decomposed into LCP and RCP components. This results in the simultaneous generation of two beams with different circular polarization states, without affecting the efficiency or beam quality, as the outcomes for the two polarization components are totally independent.

We used the commercial software CST Microwave Studio to simulate the response of the metasurfaces to incident terahertz waves at frequencies of 0.75 and 1.25 THz. The key step is to design the meta-units. The schematic diagram of a basic square-shaped meta-unit is shown in Fig. 1(b), where pillar "A" modulates the incident wave at a frequency of 0.75 THz, while pillars "B" modulate the incident wave at a frequency of 1.25 THz. Because pillar "A" achieves a modulation efficiency close to 1 at 0.75 THz while pillars "B" attain a modulation efficiency about 0.5 at 1.25 THz, when the numbers of pillars "A" to "B" in a meta-unit are 1 : 3, the modulation effect for 1.25 THz incidence is superior to that when the ratio is 2 : 2, ensuring a good modulation effect at 0.75 THz at the same time.

In Fig. 1(b), l_{xa} (l_{xb}) and l_{ya} (l_{yb}) represent the length and width of pillar A (B), respectively. By varying these parameters, the propagation phases φ_{lr} and φ_{rl} of pillar A (B) can be altered. The angle θ_a (θ_b) denotes the rotation angle of pillar A (B) and controls the geometric phase of pillar A (B). The meta-unit period is p = 300 μm, the height of the pillars h = 250 μm, and the thickness of the silicon substrate 750 μm. Fig. 2 shows the phase and amplitude responses for dielectric pillar dimensions ranging from 30 to 144 μm. The simulation used open boundary conditions along the $\pm z$ direction and periodic boundary conditions along both the $\pm x$ and $\pm y$ directions. From these simulations, a library of pillars having a high modulation efficiency and meeting the required phase values is established to design the metasurfaces.

In this work, the metasurfaces designed by combining the propagation phase and geometric phase are primarily used to generate two types of non-diffractive beams: Bessel beams and AAF beams. Bessel beams are characterized by long-distance diffraction-free propagation with a uniform intensity distribution. AAF (ring-Airy) beams, composed of Airy beams arranged in a ring pattern, self-accelerate during propagation and shrink the ring until it collapses into a point near the focus, causing a sharp increase in energy. Although the diffraction-free nature of AAF beams may not be immediately visible, it arises from the stable intensity of the main lobe of the Airy beams over a certain distance and the energy concentration at the focus. These two beam types exhibit contrasting characteristics.

The phase distribution of a Bessel beam is described by [45]:

$$\varphi_{\mathrm{b}}(x,y) = -\frac{2\pi}{\lambda}\sqrt{x^2+y^2}\mathrm{NA} \tag{2}$$

Here, x and y represent the spatial coordinates. Since the dielectric pillars in the design are grouped into supercells of 2×2, for convenience, the spatial coordinates x and y used in the phase calculations are taken as the coordinates of the supercell center. The wavelength λ is 400 μm at 0.75 THz and 240 μm at 1.25 THz. When the metasurface generates a Bessel beam, its phase distribution can be considered as the discretized phase distribution of an equivalent axicon, which is a commonly used device to generate Bessel beams. In Eq. (2), NA denotes the numerical aperture of the equivalent axicon, which is related to

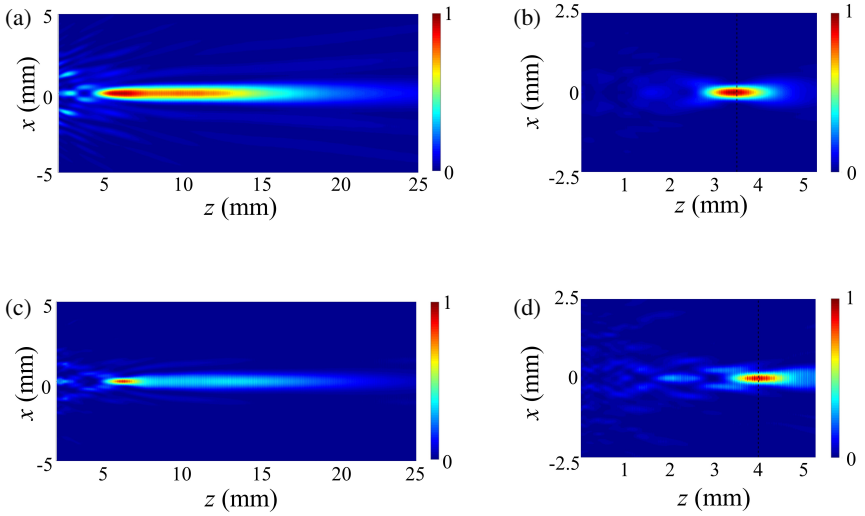

FIGURE 3. Simulation results for the metasurface designed for linear polarization. Normalized intensity profiles in the *xoz* plane for (a) x-polarization at 0.75 THz, (b) y-polarization at 0.75 THz, (c) y-polarization at 1.25 THz, and (d) x-polarization at 1.25 THz. The dashed lines in (b) and (d) indicate the focal positions of the AAF beams at 0.75 THz and 1.25 THz, respectively.

the base angle θ_{axicon} as follows [40]:

$$\text{NA} = \sin(\sin^{-1}(n_{\text{mat}} \sin(\theta_{\text{axicon}})) - \theta_{\text{axicon}}) \tag{3}$$

Here, n_{mat} represents the refractive index of the material, and set as $n_{\text{mat}} = 3.4496$ (silicon in this work).

To calculate the parameters of the equivalent axicon for the designed metasurfaces in this work, we first set the phase at the center position φ_{b} (0,0) = 0, with the period of the meta-unit chosen as 300 μm. The required phase of the meta-unit closest to the center position is chosen to be $\varphi_{\text{b}}(300, 0) = -\pi/4$. By substituting these values into Eq. (2), we get NA = $\lambda/2400$. For the 0.75 THz case, NA = 1/6, and for the 1.25 THz case, NA = 1/10. Using Eq. (3), the axicon angles are calculated as $\theta_{\text{axicon0.75}} = 3.87°$ and $\theta_{\text{axicon1.25}} = 2.33°$.

Another non-diffractive beam that is considered in this work is an AAF beam with phase distribution described by [46]:

$$\varphi_{\text{AAF}} = \begin{cases} -\frac{2\pi}{\lambda} \frac{m^2}{(2m-1)(m-1)} \left[(m-1)a\right]^{\frac{1}{m}} (r-r_0)^{\frac{2m-1}{m}}, \\ r_0 \le r \\ 0, \quad r < r_0 \end{cases} \tag{4}$$

The AAF beam is produced by rotating an Airy beam with a trajectory $c(z) = r_0 - az^{\text{m}}$ one full turn around the z-axis, the propagation direction. Here, r_0 represents the initial distance of the Airy beam from the center, a a parameter determining the trajectory of the Airy beam, m the order of the trajectory, and $r = \sqrt{x^2 + y^2}$ the spatial coordinates. The AAF beam focuses abruptly after a certain propagation distance, calculated using its trajectory equation. When the right side of the trajectory equation equals zero, i.e., $r_0 - az^m = 0$, all the Airy beam components forming the AAF beam have converged on the z-axis. At this point, the intensity of the light is maximal, referred to as the focal point. The focal length of the AAF beam is $f = (r_0/a)^{1/m}$. For the AAF beam designed in this work, the order of the beam m is 2, and the focal length is thus $f = (r_0/a)^{1/2}$.

The phase distribution Eq. (4) can be simplified to:

$$\varphi_{\text{AAF}} = \begin{cases} -\frac{8\pi}{3\lambda} a^{\frac{1}{2}} (r - r_0)^{\frac{3}{2}}, & r_0 \le r \\ 0, & r < r_0 \end{cases} \tag{5}$$

3. SIMULATION RESULTS

On the basis of the principles outlined above, we have designed several types of dual non-diffractive beam generators, each with distinct effects. These generators consist of meta-units arranged in a grid of 21 × 21, where each meta-unit has a period of 300 μm. In the simulation of the beam generators, open boundary conditions were used in the $\pm x$, $\pm y$, and $\pm z$ directions, and the incident light was set as a Gaussian beam with a waist radius of 3 mm to be consistent with the experimental conditions.

First, a special case is considered, where only propagation phase is used without geometric phase, by designing a metasurface that can generate distinct non-diffractive beams for different linearly polarized incidences. In this case, the difference in efficiency between units A and B is small, so the ratio of A to B can be designed as 2 : 2, and unit B in the bottom right corner of Fig. 1(b) can be replaced with unit A. Fig. 3 presents the simulation results of the designed metasurface. Figs. 3(a) and 3(b) illustrate the intensity profiles in the *xoz* plane at an incident frequency of 0.75 THz for x- and y-polarized waves, respectively. It is evident that a Bessel beam is generated under x-polarization, whereas an AAF beam with a focal length of approximately 3.5 mm is produced under y-polarization. The dashed line in Fig. 3(b) indicates the z-axis position at 3.5 mm. When the frequency of the incident wave is 1.25 THz, the results for x- and y-polarizations are switched, as depicted in Fig. 3(c) and 3(d). Fig. 3(c) shows the intensity profile for y-polarization, and Fig. 3(d) for x-polarization, both in the *xoz* plane. To highlight the differences in the beams, the focal point

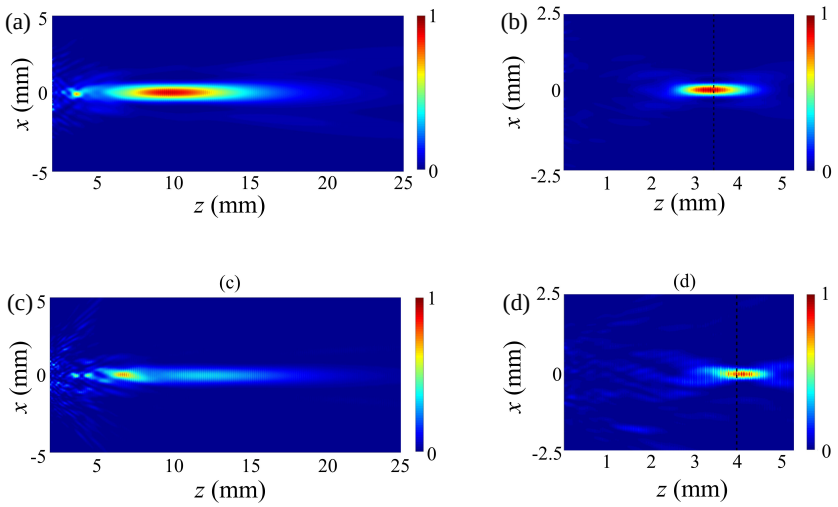

FIGURE 4. Simulation results for the metasurface designed for circular polarization to produce two straight propagating non-diffractive beams. Normalized intensity profiles in the *xoz* plane for (a) LCP at 0.75 THz, (b) RCP at 0.75 THz, (c) RCP at 1.25 THz, and (d) LCP at 1.25 THz. The dashed lines in (b) and (d) indicate the focal positions of the AAF beams at 0.75 THz and 1.25 THz, respectively.

of the AAF beam at 1.25 THz is different from that at 0.75 THz, with the focal point being approximately 4 mm, as indicated by the dashed line in Fig. 3(d). These results show that in the design the four beams generated under x- and y-polarizations at incident frequencies of 0.75 THz and 1.25 THz are indeed mutually independent. This independence will be further elucidated in the subsequent metasurface design for circular polarization. To characterize the efficiency of the proposed devices, we simulate the intensity distribution through the silicon substrate only and use it as the reference intensity I_{ref}. To calculate the efficiency, the intensity distribution transmitted through a metasurface is divided by I_{ref}, yielding the efficiency of this metasurface. The efficiencies of the beam generators in Figs. 3(a)–(d) are 57.3%, 56.1%, 49.4%, and 48.1%, respectively.

After the case for linear polarization, the main focus is on designing devices that generate non-diffractive beams under different circularly polarized incidences. The first generator is to produce a Bessel beam for an LCP wave at a frequency of 0.75 THz and an AAF beam at 1.25 THz. Conversely, when the polarization state of the incident wave is switched to RCP, an AAF beam is emitted at 0.75 THz and a Bessel beam at 1.25 THz. The simulation results in the *xoz* plane for this generator are shown in Fig. 4. Figs. 4(a) and 4(b) show the simulated intensity distributions for 0.75 THz LCP and RCP incident waves, respectively, while Figs. 4(c) and 4(d) are for 1.25 THz RCP and LCP incident waves, respectively. All results are for cross-polarization, meaning that the beam generated by LCP incident light is RCP light, and vice versa. This and the other metasurfaces discussed later have the same focal points as the case for linear polarization (namely, 3.5 mm and 4 mm) and are indicated by the dashed lines. The efficiencies of the beam generators in Figs. 4(a)–(d) are 55.9%, 56.9%, 50.2%, and 51.8%, respectively.

Next, a metasurface capable of generating non-diffractive beams in an arbitrary direction is designed. The phase distribution of this metasurface is described by:

$$\varphi_d = \varphi_{\text{beam}} \pm \frac{2\pi x}{T_x} \pm \frac{2\pi y}{T_y} \tag{6}$$

Here, φ_{beam} represents the phase distribution of the Bessel or AAF beam, and $2\pi x/T_x$ ($2\pi y/T_y$) denotes the phase required for the beam to be deflected in the x (y) direction, where T_x (T_y) represents the period of the phase gradient along the x (y) direction. The deflection angles can thus be described by:

$$\theta_{dx} = \arcsin\left(\frac{\lambda}{T_x}\right), \quad \theta_{dy} = \arcsin\left(\frac{\lambda}{T_y}\right) \tag{7}$$

Figure 5 shows the simulation results for this metasurface. With T_x (T_y) $= 2400\,\mu$m, the calculated deflection angle θ_{dx} (θ_{dy}) is 9.59° at 0.75 THz and 5.74° at 1.25 THz. Figs. 5(a) and 5(b) represent the cases for LCP and RCP incident waves at 0.75 THz, respectively. In Fig. 5(a), $T_x = 2400\,\mu$m, $T_y = 0\,\mu$m, and the Bessel beam is deflected approximately by 10.5° towards the positive x-axis, while in Fig. 5(b), $T_x = 0\,\mu$m, $T_y = 2400\,\mu$m, and the AAF beam is deflected approximately by 9.8° towards the positive y-axis. Figs. 5(c) and 5(d) represent the cases for RCP and LCP at 1.25 THz, respectively. In Fig. 5(c), $T_x = 0\,\mu$m, $T_y = -2400\,\mu$m, and the Bessel beam is deflected approximately by 7.2° towards the negative y-axis, while in Fig. 5(d), $T_x = -2400\,\mu$m, $T_y = 0\,\mu$m, and the AAF beam is deflected approximately by 6.9° towards the negative x-axis. These deflection angles are in good agreement with theoretical calculations. The efficiencies of the beam generators in Figs. 5(a)–(d) are 58.4%, 55.5%, 51.5%, and 49.8%, respectively.

In the above designs, for incident waves with the same frequency and polarization, only one non-diffractive beam is generated. To meet the demands in practical applications, a metasurface capable of generating two non-diffractive beams simultaneously is designed. The required phase for this metasurface,

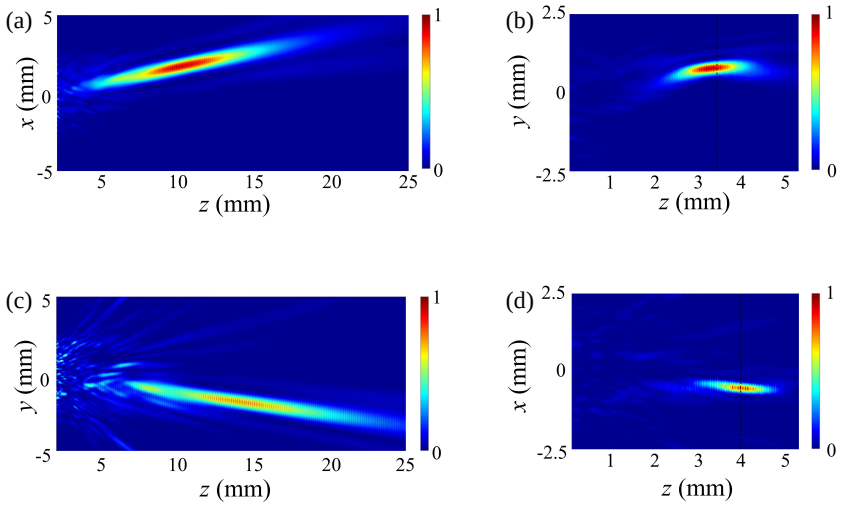

FIGURE 5. Simulation results for the metasurface designed with unidirectional deflection. Normalized intensity profiles in the *xoz* plane for (a) LCP at 0.75 THz and (d) LCP at 1.25 THz, as well as in the *yoz* plane for (b) RCP at 0.75 THz and (c) RCP at 1.25 THz. The dashed lines in (b) and (d) indicate the focal positions of the AAF beams at 0.75 THz and 1.25 THz, respectively.

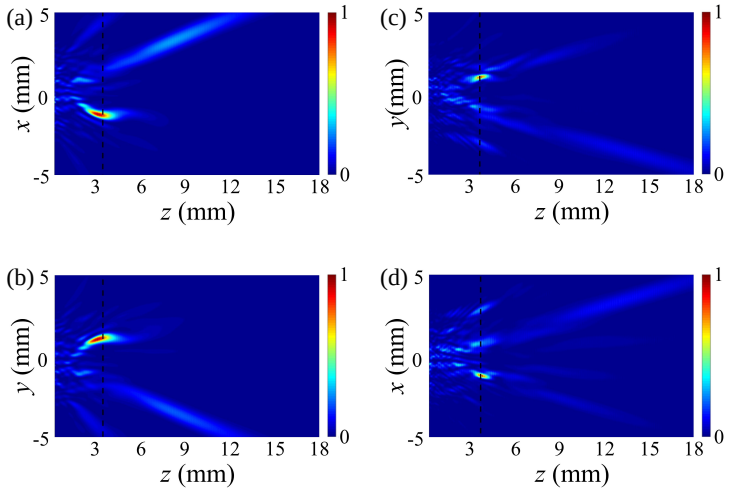

FIGURE 6. Simulation results for the metasurface that can generate two beams simultaneously. Normalized intensity profiles in the *xoz* plane for (a) LCP at 0.75 THz and (d) LCP at 1.25 THz, as well as in the *yoz* plane for (b) RCP at 0.75 THz and (c) RCP at 1.25 THz. The dashed lines indicate the focal positions of the AAF beams.

φ_{sum}, can be described by [47]:

$$\varphi_{\text{sum}} = \arg\left\{\exp\left[\mathrm{i}\left(\varphi_{\text{beam},1} + a_1\frac{2\pi x}{T_x} + b_1\frac{2\pi y}{T_y}\right)\right] + \exp\left[\mathrm{i}\left(\varphi_{\text{beam},2} + a_2\frac{2\pi x}{T_x} + b_2\frac{2\pi y}{T_y}\right)\right]\right\} \quad (8)$$

Here, the values of a_1, b_1, a_2, and b_2 are 0 or ± 1, which are parameters controlling the deflection directions of the beams; T_x and T_y represent the phase gradient periods along the x and y directions, respectively.

Figure 6 shows the simulation results for this metasurface that can generate two beams simultaneously. With $T_x = T_y = 1200\,\mu\text{m}$, the calculated deflection angles at 0.75 THz and 1.25 THz are $\theta_d = 19.47°$ and 11.53°, respectively, while the corresponding angles in Fig. 6 are 20.4° and 13.8°. Fig. 6(a) depicts the result for LCP light at 0.75 THz, where a Bessel beam deflecting in the positive x-axis and an AAF beam deflecting in the negative x-axis can be observed. Fig. 6(b) shows the result for RCP light, where a Bessel beam deflecting in the negative y-axis and an AAF beam deflecting in the positive y-axis can be seen. In comparison, Fig. 6(c) shows the result for RCP light at 1.25 THz, where the Bessel beam deflects in the negative y-axis and the AAF beam in the positive y-axis. Fig. 6(d) shows the result for LCP light, where the Bessel beam deflects in the positive x-axis and the AAF beam in the negative x-axis. The generation efficiencies for the Bessel beams in Figs. 6(a)–(d) are 29.0%, 28.7%, 24.5%, and 25.6%, respectively, and those for the AAF beams are 29.4%, 28.0%, 26.3%, and 25.9%, respectively. The values are around half of those for the previous devices because the energy is divided into two beams.

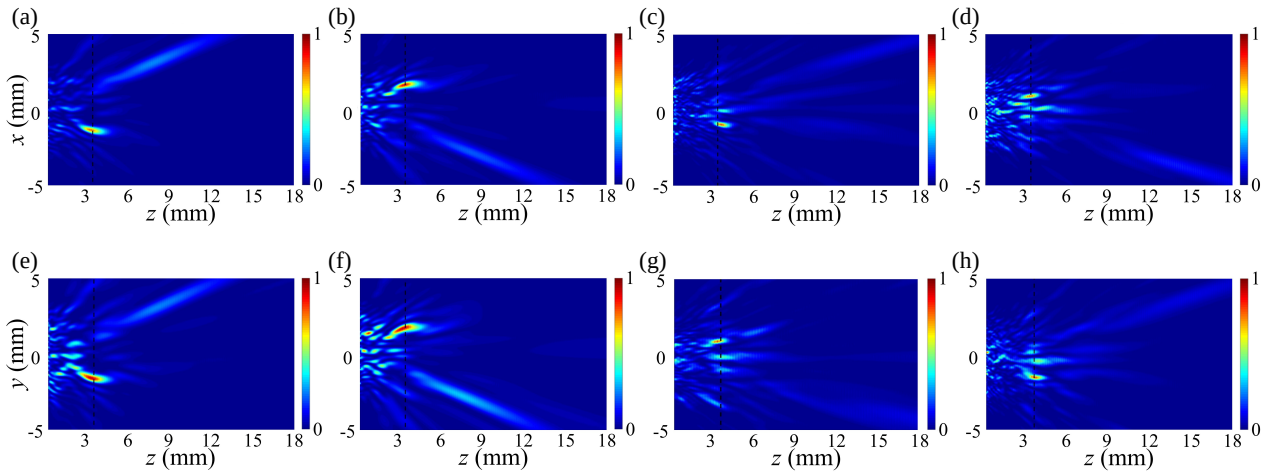

FIGURE 7. Simulation results for the metasurface that can generate four beams simultaneously. Normalized intensity profiles in the *xoz* plane for (a) LCP at 0.75 THz, (b) RCP at 0.75 THz, (c) LCP at 1.25 THz, and (d) RCP at 1.25 THz, as well as in the *yoz* plane for (e) LCP at 0.75 THz, (f) RCP at 0.75 THz, (g) LCP at 1.25 THz, and (h) RCP at 1.25 THz. The dashed lines indicate the focal positions of the AAF beams.

The simulation results in Fig. 6 show that the effect of generating two different beams simultaneously is very good. To fully explore the degrees of freedom enabled by the meta-atoms, a four beam generator is designed. By extending Eq. (8), the required phase for a metasurface capable of generating four beams simultaneously can be obtained:

$$\varphi_{\text{sum}} = \arg\left\{\sum_{n=1}^{4} \exp\left[\mathrm{i}\left(\varphi_{\text{beam,n}} + a_n \frac{2\pi x}{T_x} + b_n \frac{2\pi y}{T_y}\right)\right]\right\} \quad (9)$$

where arg stands for the argument. With $T_x = T_y = 1200\,\mu\text{m}$, the deflection angles for the four-beam metasurface are the same as those for the dual-beam metasurface shown in Fig. 6. The four beams generated include one Bessel beam and one AAF beam in the *xoz* plane, and another pair of Bessel and AAF beams in the *yoz* plane. Figs. 7(a) and 7(e) show respectively the intensity distributions in the *xoz* and *yoz* planes for incident LCP waves at 0.75 THz, where in Fig. 7(a) the Bessel beam is deflected in the positive x-axis and the AAF beam in the negative x-axis, while in Fig. 7(e) the Bessel beam is deflected in the positive y-axis and the AAF beam in the negative y-axis. Figs. 7(b) and 7(f) show respectively the intensity distributions in the *xoz* and *yoz* planes for incident RCP waves at 0.75 THz. In Fig. 7(b) the Bessel beam is deflected in the negative x-axis and the AAF beam in the positive x-axis, while in Fig. 7(f) the Bessel beam is deflected in the negative y-axis and the AAF beam in the positive y-axis. In comparison, Figs. 7(c) and 7(g) show respectively the intensity distributions in the *xoz* and *yoz* planes for incident LCP waves at 1.25 THz, where in Fig. 7(c) the Bessel beam is deflected in the positive x-axis and the AAF beam in the negative x-axis, while in Fig. 7(g) the Bessel beam is deflected in the negative y-axis and the AAF beam in the positive y-axis. Figs. 7(d) and 7(h) show respectively the intensity distributions in the *xoz* and *yoz* planes for incident RCP waves at 1.25 THz, where in Fig. 7(d) the Bessel beam is deflected in the negative x-axis and the AAF beam in the positive x-axis, while in Fig. 7(h) the Bessel beam is deflected in the positive y-axis and the AAF beam in the negative y-axis. From the simulation results in Fig. 7, it can be seen that although the quality of beam generation is sightly diminished, four different beams distributed in the *xoz* and *yoz* planes can be clearly distinguished. The generation efficiencies for the Bessel beams in Figs. 7(a)–(d) are 14.4%, 14.3%, 12.4%, and 12.0%, respectively, and those for the AAF beams are 15.1%, 14.2%, 12.8%, and 12.6%, respectively. The generation efficiencies for the Bessel beams in Figs. 7(e)–(h) are 14.8%, 15.0%, 12.7%, and 11.9%, respectively, and those for the AAF beams in Figs. 7(e)–(h) are 14.8%, 13.4%, 12.1%, and 12.8%, respectively.

4. EXPERIMENTAL RESULTS AND DISCUSSION

To experimentally demonstrate the feasibility of the dual non-diffractive terahertz beam generators that can operate at two frequencies, all-dielectric metasurface samples based on silicon are fabricated by optical lithography followed by deep reactive ion etching (DRIE) [48]. First, a chromium layer with a thickness of approximately 10 nm was sputtered onto one side of a 4-inch-diameter, 1-mm-thick high-resistivity silicon wafer. Subsequently, a 10-µm-thick layer of AZ2070 photoresist was spin-coated onto the chromium layer. The photoresist was precisely patterned using a photomask and developed through conventional UV photolithography. The chromium layer not covered by the photoresist was then removed via acid etching. Next, DRIE was employed to etch the exposed silicon regions to a depth of 250 µm, with the remaining photoresist and chromium serving as a hard mask. The DRIE process alternated between protection and etching cycles. Finally, the residual photoresist and chromium were removed using acetone and acid cleaning, completing the metasurface fabrication. The consistency of the fabrication could be guaranteed as long as the same operation procedures were followed.

To characterize the metasurface samples, a near-field scanning terahertz microscopy system is used, which can also measure the far-field distributions, as illustrated in Fig. 8 [49]. The measurement is performed in dry air to avoid the influ-

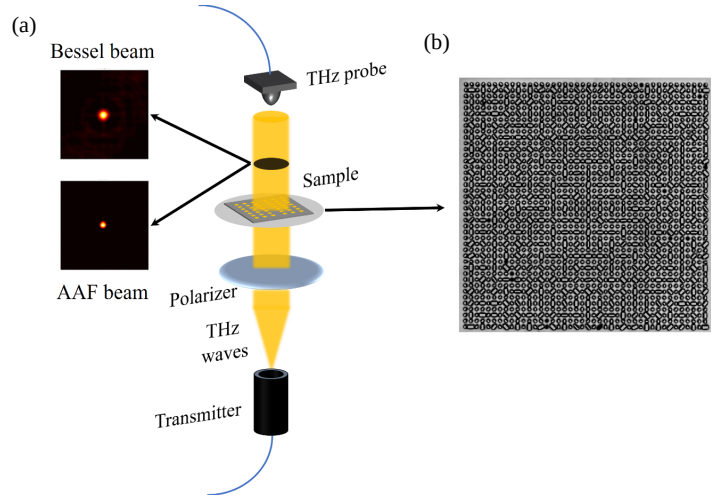

FIGURE 8. (a) Diagram of experimental setup and (b) optical microscopy image of a metasurface sample.

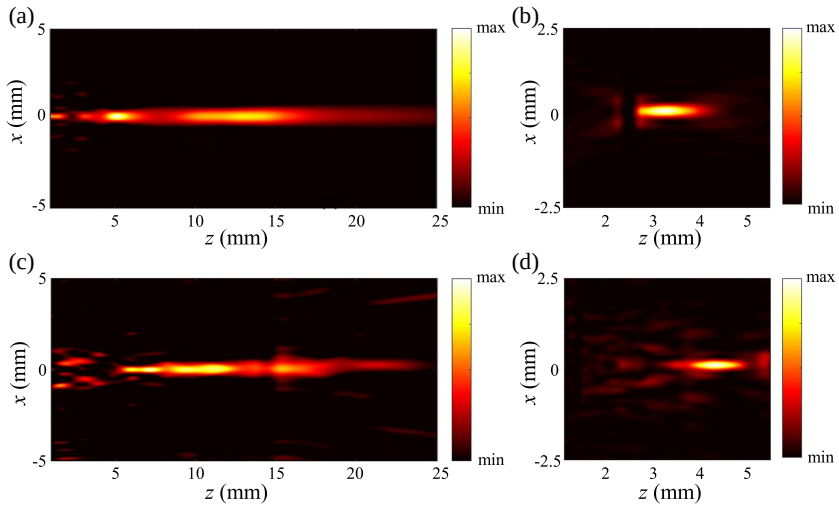

FIGURE 9. Experimental results for the metasurface designed for linear polarization. Intensity profiles in the *xoz* plane for (a) x-polarization at 0.75 THz, (b) y-polarization at 0.75 THz, (c) y-polarization at 1.25 THz, and (d) x-polarization at 1.25 THz.

ence of water vapor. In the experiment, a linearly-polarized broadband free-space terahertz beam is generated from a photoconductive antenna and then collimated by a TPX terahertz lens. During measurement, the terahertz radiation is incident onto the substrate side of the metasurface, which is placed on a three-dimensional translational sample holder. A terahertz probe, equipped with a two-dimensional translational detector capable of scanning in the x and y directions, is used to measure the electric field of the transmitted terahertz waves point by point. Due to the lack of quarter-wave plates operating at frequencies of 0.75 THz and 1.25 THz, the circularly-polarized incidences cannot be directly obtained and are thus synthesized from results from linearly-polarized incidences. A polarizer is used and rotated to +45° and $-45°$ relative to the linear polarization direction of the terahertz radiation emitted by the photoconductive antenna to measure the electric fields $E_{+45°}$ and $E_{-45°}$. These two electric fields are obtained by performing Fourier transforms to the time-domain signals at the points of measurement and are complex amplitudes over a broad frequency range. At this point, the electric field distribution with a spin of σ and a wavelength of λ can be calculated as $[E_{+45°}(\lambda) + \mathrm{i}\sigma E_{-45°}(\lambda)]/\sqrt{2}$.

The experimental results for the metasurface designed for linear polarization are presented in Fig. 9, showing the intensity distributions of the non-diffractive beams at 0.75 THz and 1.25 THz for x- and y-polarized incident waves. A comparison between the experimental results in Fig. 9 and the simulation results in Fig. 3 reveals that the characteristics of the generated Bessel beams are largely consistent for the same frequency and polarization. Additionally, the focal lengths of the generated AAF beams align with the simulation results. The efficiencies of the beam generators in Figs. 9(a)–(d) are 56.7%, 57.7%, 48.9%, and 49.0%, respectively. The calculation of the efficiency values is similar to that in simulation but with measured intensity distributions used.

The following experiments are conducted to measure the metasurface samples designed for circular polarization. Using the formulas described earlier, we obtain the intensity distribu-

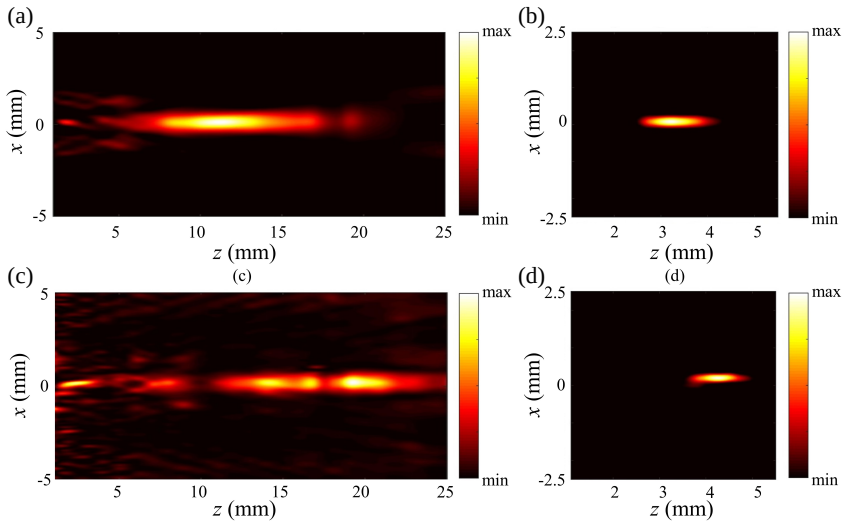

FIGURE 10. Experimental results for the metasurface designed for circular polarization to produce two straight propagating non-diffractive beams. Intensity profiles in the *xoz* plane for (a) LCP at 0.75 THz, (b) RCP at 0.75 THz, (c) RCP at 1.25 THz, and (d) LCP at 1.25 THz.

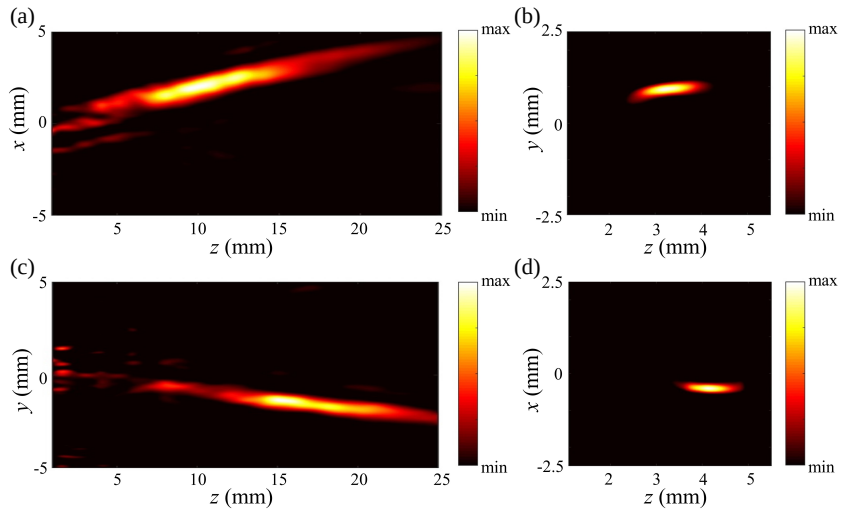

FIGURE 11. Experimental results for the metasurface designed with unidirectional deflection. Intensity profiles in the *xoz* plane for (a) LCP at 0.75 THz and (d) LCP at 1.25 THz, as well as in the *yoz* plane for (b) RCP at 0.75 THz and (c) RCP at 1.25 THz.

tions of LCP and RCP lights by measuring E_{+45° and E_{-45° fields. Fig. 10 shows the experimental results for the metasurface designed for circular polarization. It can be seen, by comparing the results in Fig. 10 and Fig. 4, that for the same circular polarization and frequency, the experimentally generated non-diffractive beams correspond well to the simulation results. The efficiencies of the beam generators in Figs. 10(a)–(d) are 57.2%, 55.2%, 53.4%, and 52.0%, respectively. Fig. 11 shows the experimental results for the metasurface designed with unidirectional deflection, corresponding to the simulation results in Fig. 5. The deflection angles in Figs. 11(a)–(d) are 11.5°, 8.9°, 6.4°, and 6.2°, respectively, close to the simulation results and theoretical values. The efficiencies of the beam generators in Figs. 11(a)–(d) are 55.5%, 54.7%, 49.5%, and 50.2%, respectively.

Figures 12 and 13 show respectively the experimental results for the metasurfaces that can simultaneously generate two and four beams for waves of the same polarization and frequency. Analysis of the intensity distributions in Fig. 12 shows clear splitting to produce one Bessel beam and one AAF beam, with the focal position of the AAF beam aligning well with expectations and the transmission of the Bessel beam being distinctly identifiable. The generation efficiencies for the Bessel beams in Figs. 12(a)–(d) are 28.5%, 26.8%, 22.6%, and 24.5%, respectively, and those for the AAF beams are 25.4%, 24.5%, 22.8%, and 23.0%. As shown in Fig. 6 and Fig. 12, the intensities at the strongest points of the generated AAF beams are significantly higher than those of the Bessel beams, which is a result of the intrinsic characteristics of the AAF beams. The AAF beams have the property of abrupt self-focusing, with the energy increasing dramatically near the focal point. However, this does not imply that the functionality of the generated Bessel beams is affected. However, upon analyzing Fig. 13, we can see that when two Bessel beams and two AAF beams are produced simultaneously, the quality of the generated non-diffractive beams shows obvious decreases compared with the results in Fig. 12

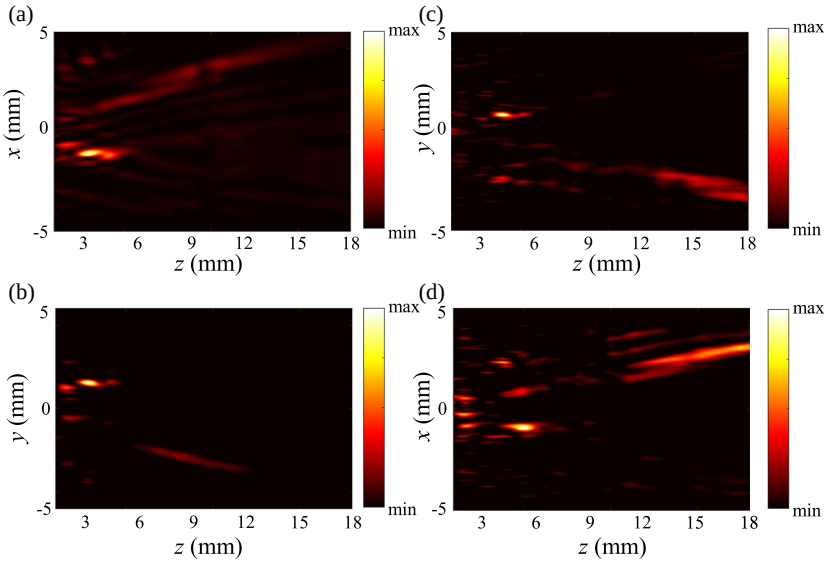

FIGURE 12. Experimental results for the metasurface that can generate two beams simultaneously. Intensity profiles in the *xoz* plane for (a) LCP at 0.75 THz and (d) LCP at 1.25 THz, as well as in the *yoz* plane for (b) RCP at 0.75 THz and (c) RCP at 1.25 THz.

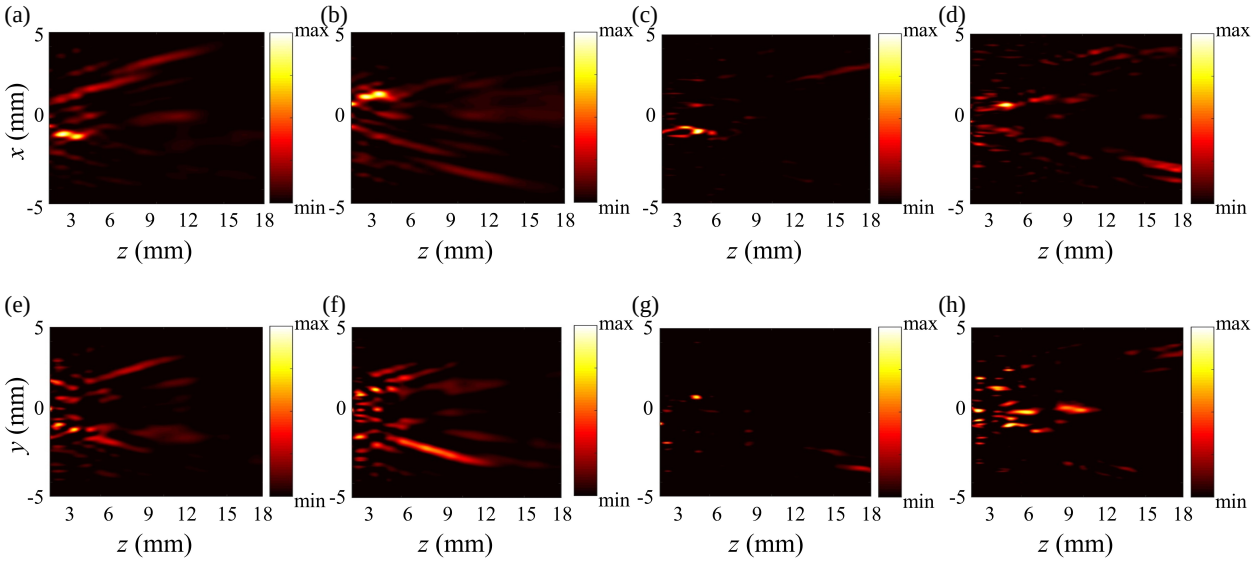

FIGURE 13. Experimental results for the metasurface that can generate four beams simultaneously. Intensity profiles in the *xoz* plane for (a) LCP at 0.75 THz, (b) RCP at 0.75 THz, (c) LCP at 1.25 THz, and (d) RCP at 1.25 THz, as well as in the *yoz* plane for (e) LCP at 0.75 THz, (f) RCP at 0.75 THz, (g) LCP at 1.25 THz, and (h) RCP at 1.25 THz.

for the two-beam metasurface and the corresponding simulations in Fig. 7. This decline is due to the dispersion of light energy among four output beams, resulting in each beam having half the intensity of the beams in Fig. 12. In the experiments, the use of linear polarizers rotated to $\pm 45^\circ$ to measure the electric fields due to the absence of suitable quarter-wave plates inevitably introduces interference from light that is not properly converted, which significantly affects the results when four beams are produced. Thus, in Eq. (9), the value of n should not be too large. The efficiency values are not calculated for the beams in Fig. 13 due to the sub-optimal beam quality.

This work reports metasurface designs for the generation of Bessel and AAF beams, with the added feature of beam deflection. Comparing simulations with experimental results, key parameters include the diffraction-free propagation distances of the Bessel beams, the focal positions of the AAF beams, and the deflection angles. While the simulation aligns with design parameters (metasurface dimensions, incident terahertz field distribution, and beam waist radius), experimental deviations arise mainly due to fabrication errors and changes in incident light field conditions. Despite these minor discrepancies, such as small variations in deflection angles and focal points, the results show no significant differences, and the basic device functionality remains unaffected.

To compare with similar metasurface devices that have been reported, we have listed in Table 1 key parameters, including

TABLE 1. Comparison of key metrics between our design and reported metasurfaces.

Reference No.	Mode of Operation	Frequency Range/ Wavelength	Polarization multiplexing	Number of layers	Efficiency
Ref. [31]	Transmissive and reflective	7 and 17 GHz	No	Multi-	$\sim$ 80% (reflective) $\sim$ 40% (transmissive)
Ref. [32]	Transmissive	800 nm	No	Single-	$\sim$ 40%
Ref. [33]	Transmissive and reflective	5.8–9.8 GHz	Yes	Multi-	$\sim$ 50%–90%
Ref. [37]	Reflective	30 GHz	No	Multi-	13.1%
Ref. [42]	Reflective	525 and 633 nm	Yes	Single-	18.9% (525 nm) 7.32% (633 nm)
Ref. [44]	Transmissive	0.6 THz	Yes	Multi-	>70%
Our design	Transmissive	0.75 and 1.25 THz	Yes	Single-	$\sim$ 50%

mode of operation (reflection or transmission), operation frequency range or wavelength, polarization multiplexing characteristic, number of layers, and efficiency. Among them, transmission-type devices are more convenient for practical use and measurement; the operation frequency range or wavelength indicates whether the device operates at multiple frequencies; polarization multiplexing, if present, allows for composite manipulation; single-layer devices are easier to fabricate, while multi-layer devices are more difficult to process; and higher efficiency means better energy utilization. It can be seen that our device can be measured using a relatively simple transmission-type measurement system, operates at two frequencies, supports polarization multiplexing, is easier to fabricate as a single-layer device, and exhibits fairly good efficiency. In addition, our devices have a certain bandwidth for operation, maintaining high efficiency within the frequency ranges of 0.75 THz $\pm$ 0.1 THz and 1.25 THz $\pm$ 0.1 THz. Both our devices and reference [44] focus on all-dielectric terahertz metasurfaces, but the efficiency of our devices is lower than that in [44] mainly because [44] designed a single anti-reflection layer. The same technique can be adopted for our design. While this would make our design a multi-layer structure, it differs from the multi-layer devices listed in the table. The multi-layer devices in our case will be processed with different structures on both sides of a wafer, which only slightly complicates the fabrication process compared to single-layer devices. In contrast, the multi-layer metasurfaces in other references are mostly three-layer structures, with metal unit cells, which are much more complex to fabricate than the all-dielectric structures used in our design.

5. CONCLUSION

In this work, we have demonstrated all-silicon dielectric metasurfaces capable of generating switchable two distinct non-diffractive beams for incident waves with varying frequencies and polarization states, that is, Bessel beams with long-distance non-diffractive propagation characteristics and AAF beams with abruptly concentrated energy during transmission. By applying appropriate phase modulation, additional operations such as deflection and beam splitting can be performed on these non-diffractive beams. The proposed design concept is validated through experiments, showing good agreement with simulations. Such multifunctional devices hold tremendous potential in terahertz imaging, non-destructive testing, biomedical fields, and many other applications.

DECLARATION OF COMPETING INTEREST

The authors declare that they have no known competing financial interests or personal relationships that could have appeared to influence the work reported in this paper.

ACKNOWLEDGEMENT

This work was supported by the National Natural Science Foundation of China (61875150, 61935015, 62025504, 62005193, and 62275195).

REFERENCES

[1] Durnin, J., J. Miceli, Jr., and J. H. Eberly, "Diffraction-free beams," *Physical Review Letters*, Vol. 58, No. 15, 1499–1501, 1987.

[2] Gori, F., G. Guattari, and C. Padovani, "Bessel-Gauss beams," *Optics Communications*, Vol. 64, No. 6, 491–495, 1987.

[3] Siviloglou, G. A. and D. N. Christodoulides, "Accelerating finite energy Airy beams," *Optics Letters*, Vol. 32, No. 8, 979–981, 2007.

[4] Efremidis, N. K. and D. N. Christodoulides, "Abruptly autofocusing waves," *Optics Letters*, Vol. 35, No. 23, 4045–4047, 2010.

[5] Cottrell, D. M., J. A. Davis, and T. M. Hazard, "Direct generation of accelerating Airy beams using a 3/2 phase-only pattern," *Optics Letters*, Vol. 34, No. 17, 2634–2636, 2009.

[6] Aruga, T., "Generation of long-range nondiffracting narrow light beams," *Applied Optics*, Vol. 36, No. 16, 3762–3768, 1997.

[7] Arlt, J. and K. Dholakia, "Generation of high-order bessel beams by use of an axicon," *Optics Communications*, Vol. 177, No. 1-6, 297–301, 2000.

[8] Brzobohatý, O., T. Čižmár, and P. Zemánek, "High quality quasi-Bessel beam generated by round-tip axicon," *Optics Express*, Vol. 16, No. 17, 12 688–12 700, 2008.

[9] Deng, F., Z. Guo, M. Ren, X. Su, L. Dong, Y. Liu, Y. Shi, and H. Chen, "Bessel beam generated by the zero-index metalens," *Progress In Electromagnetics Research*, Vol. 174, 89–106, 2022.

[10] Zhi, Z., Q. Na, Q. Xie, B. Chen, Y. Li, X. Liu, X. Li, L. Wang, G. Lo, and J. Song, "On-chip generation of Bessel-Gaussian beam via concentrically distributed grating arrays for long-range sensing," *Light: Science & Applications*, Vol. 12, No. 1, 92, 2023.

[11] Moura, T. A., U. M. S. Andrade, J. B. S. Mendes, and M. S. Rocha, "Modulating the trapping and manipulation of semiconductor particles using Bessel beam optical tweezers," *Optics and Lasers in Engineering*, Vol. 170, 107778, 2023.

[12] Yuan, Y., T. Lei, Z. Li, Y. Li, S. Gao, Z. Xie, and X. Yuan, "Beam wander relieved orbital angular momentum communication in turbulent atmosphere using Bessel beams," *Scientific Reports*, Vol. 7, No. 1, 42276, 2017.

[13] McGloin, D. and K. Dholakia, "Bessel beams: Diffraction in a new light," *Contemporary Physics*, Vol. 46, No. 1, 15–28, 2005.

[14] Scott, G. and N. McArdle, "Efficient generation of nearly diffraction-free beams using an axicon," *Optical Engineering*, Vol. 31, No. 12, 2640–2643, 1992.

[15] Bhuyan, M. K., F. Courvoisier, P. A. Lacourt, M. Jacquot, R. Salut, L. Furfaro, and J. M. Dudley, "High aspect ratio nanochannel machining using single shot femtosecond Bessel beams," *Applied Physics Letters*, Vol. 97, No. 8, 081102, 2010.

[16] Mondal, S. K., S. S. Pal, and P. Kapur, "Optical fiber nano-tip and 3D bottle beam as non-plasmonic optical tweezers," *Optics Express*, Vol. 20, No. 15, 16 180–16 185, 2012.

[17] Dufour, P., M. Piché, Y. D. Koninck, and N. McCarthy, "Two-photon excitation fluorescence microscopy with a high depth of field using an axicon," *Applied Optics*, Vol. 45, No. 36, 9246–9252, 2006.

[18] Bitman, A., I. Moshe, and Z. Zalevsky, "Improving depth-of field in broadband THz beams using nondiffractive Bessel beams," *Optics Letters*, Vol. 37, No. 19, 4164–4166, 2012.

[19] Papazoglou, D. G., N. K. Efremidis, D. N. Christodoulides, and S. Tzortzakis, "Observation of abruptly autofocusing waves," *Optics Letters*, Vol. 36, No. 10, 1842–1844, 2011.

[20] Zhang, P., J. Prakash, Z. Zhang, M. S. Mills, N. K. Efremidis, D. N. Christodoulides, and Z. Chen, "Trapping and guiding microparticles with morphing autofocusing Airy beams," *Optics Letters*, Vol. 36, No. 15, 2883–2885, 2011.

[21] Liu, K., A. D. Koulouklidis, D. G. Papazoglou, S. Tzortzakis, and X.-C. Zhang, "Enhanced terahertz wave emission from air-plasma tailored by abruptly autofocusing laser beams," *Optica*, Vol. 3, No. 6, 605–608, 2016.

[22] Panagiotopoulos, P., D. G. Papazoglou, A. Couairon, and S. Tzortzakis, "Sharply autofocused ring-Airy beams transforming into non-linear intense light bullets," *Nature Communications*, Vol. 4, No. 1, 2622, 2013.

[23] Miao, J., Z. Zhou, Y. Liu, C. Lin, X. Zhu, Z. Sun, and X. Yu, "Terahertz Bessel metalens with an extended non-diffractive length and a high efficiency," *Optics Letters*, Vol. 48, No. 19, 5117–5120, 2023.

[24] Li, H., X. Chen, L. Zhao, X. Meng, and T. Wu, "Scattering characteristics of a terahertz Bessel vortex beam by 3D dielectric-coated targets," *Applied Optics*, Vol. 62, No. 7, 1865–1870, 2023.

[25] Huang, H.-F. and J.-Y. Wang, "Switchable terahertz orbital angular momentum Bessel beams based on spin-decoupled multifunctional reflective metasurfaces," *Optics Express*, Vol. 31, No. 21, 34 855–34 870, 2023.

[26] Yu, N., P. Genevet, M. A. Kats, F. Aieta, J.-P. Tetienne, F. Capasso, and Z. Gaburro, "Light propagation with phase discontinuities: Generalized laws of reflection and refraction," *Science*, Vol. 334, No. 6054, 333–337, 2011.

[27] Pors, A. and S. I. Bozhevolnyi, "Plasmonic metasurfaces for efficient phase control in reflection," *Optics Express*, Vol. 21, No. 22, 27 438–27 451, 2013.

[28] Ni, X., N. K. Emani, A. V. Kildishev, A. Boltasseva, and V. M. Shalaev, "Broadband light bending with plasmonic nanoantennas," *Science*, Vol. 335, No. 6067, 427, 2012.

[29] Zhou, Y., T. Zhang, G. Wang, Z. Guo, X. Zang, Y. Zhu, F. Ding, and S. Zhuang, "Directional phase and polarization manipulation using Janus metasurfaces," *Advanced Science*, Vol. 11, No. 38, 2406571, 2024.

[30] Ding, F., C. Meng, and S. I. Bozhevolnyi, "Electrically tunable optical metasurfaces," *Photonics Insights*, Vol. 3, No. 3, R07, 2024.

[31] Bao, L., X. Fu, R. Y. Wu, Q. Ma, and T. J. Cui, "Full-space manipulations of electromagnetic wavefronts at two frequencies by encoding both amplitude and phase of metasurface," *Advanced Materials Technologies*, Vol. 6, No. 4, 2001032, 2021.

[32] Cui, G., M. Gu, C. Cheng, Z. Zhang, Y. Zhou, Q. Dong, S. Gao, D.-Y. Choi, C. Cheng, and C. Liu, "Multifunctional all-dielectric quarter-wave plate metasurfaces for generating focused vector beams of Bell-like states," *Nanophotonics*, Vol. 13, No. 9, 1631–1644, 2024.

[33] Yang, H., Y. He, M. S. Tong, L. T. Guo, P. Li, and Y. J. Zhang, "A reflection-transmission multifunctional polarization conversion metasurface," *IEEE Transactions on Antennas and Propagation*, Vol. 72, No. 6, 5099–5109, 2024.

[34] Cheng, H.-Y., M.-J. Ye, W.-R. Chen, C.-Y. Yang, S.-W. Chu, K.-P. Chen, and K.-H. Lin, "Large optical modulation of dielectric Huygens' metasurface absorber," *Advanced Optical Materials*, Vol. 11, No. 10, 2300102, 2023.

[35] Zhou, J., H. Qian, H. Luo, S. Wen, and Z. Liu, "A spin controlled wavefront shaping metasurface with low dispersion in visible frequencies," *Nanoscale*, Vol. 11, No. 36, 17 111–17 119, 2019.

[36] Jin, L., J. Xie, B. Pan, and G. Luo, "Generalized phase retrieval model based on physics-inspired network for holographic metasurface," *Progress In Electromagnetics Research*, Vol. 178, 103–110, 2023.

[37] Huang, H.-F. and H. Huang, "Millimeter-wave wideband high efficiency circular airy OAM multibeams with multiplexing OAM modes based on transmission metasurfaces," *Progress In Electromagnetics Research*, Vol. 173, 151–159, 2022.

[38] Genevet, P., F. Capasso, F. Aieta, M. Khorasaninejad, and R. Devlin, "Recent advances in planar optics: From plasmonic to dielectric metasurfaces," *Optica*, Vol. 4, No. 1, 139–152, 2017.

[39] Staude, I. and J. Schilling, "Metamaterial-inspired silicon nanophotonics," *Nature Photonics*, Vol. 11, No. 5, 274–284, 2017.

[40] Liu, C., Y. Li, X. Feng, X. Zhang, J. Han, and W. Zhang, "Dual non-diffractive terahertz beam generators based on all-dielectric metasurface," *Frontiers of Optoelectronics*, Vol. 14, No. 2, 201–210, 2021.

[41] Zhang, H., X. Zhang, Q. Xu, C. Tian, Q. Wang, Y. Xu, Y. Li, J. Gu, Z. Tian, C. Ouyang, *et al.*, "High-efficiency dielectric metasurfaces for polarization-dependent terahertz wavefront manipulation," *Advanced Optical Materials*, Vol. 6, No. 1, 1700773, 2018.

[42] Ren, R., Z. Li, L. Deng, X. Shan, Q. Dai, Z. Guan, G. Zheng, and S. Yu, "Non-orthogonal polarization multiplexed metasurfaces for tri-channel polychromatic image displays and information encryption," *Nanophotonics*, Vol. 10, No. 11, 2903–2914, 2021.

[43] Liu, M., W. Zhu, P. Huo, L. Feng, M. Song, C. Zhang, L. Chen, H. J. Lezec, Y. Lu, A. Agrawal, and T. Xu, "Multifunctional metasurfaces enabled by simultaneous and independent control of phase and amplitude for orthogonal polarization states," *Light: Science & Applications*, Vol. 10, No. 1, 107, 2021.

[44] Huang, F., Q. Xu, W. Liu, T. Wu, J. Gu, J. Han, and W. Zhang, "Generating superposed terahertz perfect vortices via a spin-multiplexed all-dielectric metasurface," *Photonics Research*, Vol. 11, No. 3, 431–441, 2023.

[45] Chen, W. T., M. Khorasaninejad, A. Y. Zhu, J. Oh, R. C. Devlin, A. Zaidi, and F. Capasso, "Generation of wavelength-independent subwavelength Bessel beams using metasurfaces," *Light: Science & Applications*, Vol. 6, No. 5, e16259, 2017.

[46] Zhao, Z., C. Xie, D. Ni, Y. Zhang, Y. Li, F. Courvoisier, and M. Hu, "Scaling the abruptly autofocusing beams in the direct-space," *Optics Express*, Vol. 25, No. 24, 30 598–30 605, 2017.

[47] Zhang, Y., W. Liu, J. Gao, and X. Yang, "Generating focused 3D perfect vortex beams by plasmonic metasurfaces," *Advanced Optical Materials*, Vol. 6, No. 4, 1701228, 2018.

[48] Wang, Q., Q. Xu, X. Zhang, C. Tian, Y. Xu, J. Gu, Z. Tian, C. Ouyang, X. Zhang, J. Han, and W. Zhang, "All-dielectric meta-holograms with holographic images transforming longitudinally," *ACS Photonics*, Vol. 5, No. 2, 599–606, 2018.

[49] Jiang, X., Q. Xu, Y. Lang, W. Liu, X. Chen, Y. Xu, H. Ren, X. Wang, S. Xu, X. Zhang, *et al.*, "Geometric phase control of surface plasmons by dipole sources," *Laser & Photonics Reviews*, Vol. 17, No. 6, 2200948, 2023.